Journal of Intelligent Manufacturing (2020) 31:575–596
https://doi.org/10.1007/s10845-019-01469-w

A study on the prediction of inherent deformation in fillet-welded joint using support vector machine and genetic optimization algorithm

Liang Tian[1,2,3] · **Yu Luo**[2]

Received: 21 August 2018 / Accepted: 15 February 2019 / Published online: 21 February 2019

Abstract
The inherent deformation method has a significant advantage in evaluating the total welding deformations for large and complex welded structures. The prerequisite for applying this approach is that the inherent deformations of corresponding weld joints should be known beforehand. In this study, an intelligent model based on support vector machine (SVM) and genetic algorithm (GA) was established to predict the inherent deformations of a fillet-welded joint. The training samples were obtained from numerical experiments conducted by the thermal–elastic–plastic finite element analysis. In the developed SVM model, the welding speed, current, voltage and plate thickness were considered as input parameters, and the longitudinal and transverse inherent deformations were corresponding outputs. The correlation coefficients and percentage errors for all the samples were calculated to evaluate the prediction performance of the SVM model. The research results demonstrate that the SVM model optimized by GA can be used to assess the longitudinal and transverse inherent deformations for the T-joint fillet weld with acceptable accuracy.

Keywords T-joint fillet welding · Inherent deformations · Numerical simulation · Support vector machine · Genetic algorithm · Finite element method

Introduction

Welded joints made by a fusion welding process are widely used in engineering applications to fabricate steel structures and to transmit loads from one structural component to another. There are several basic types of welded joints, such as butt, lap, fillet and corner joints, etc. Among these welded joints, T-joint fillet welds are commonly employed in various industrial applications, e.g., shipbuilding, marine industry, pressure pipelines, steel bridges and construction machinery (Radaj 1992). However, these welded structures inevitably exist welding deformations, which are caused by the melting and solidification of weld metal and base metal in a localized fusion zone by a transient thermal heat source. Welding deformations produced in welding process can have an unfavorable influence on the expected performance of welded structures. Thus, accurate estimation and reasonable prevention for welding deformations are very crucial to the high-precision manufacture and assembly of the welded structures (Ueda et al. 2012).

Effective methods for predicting welding deformations are difficult due to the complexity of the welding process which has some inherent characteristics such as moving heat source, localized heating and temperature dependence of material properties, etc. Accordingly, many numerical and experimental studies have been performed to predict welding-induced distortions in T-joint fillet welding. For example, Jung and Tsai (2004) investigated the effect of external restraints and thermal management techniques on the angular distortions in T-joints, the research results demonstrated that the external restraints and preheating could reduce angular distortions to some extent. Vakili-Tahami and Ziaei-Asl (2013) carried out a series of numerical and experimental investigations for T-shape fillet welding, and the results showed that the developed 3D model could predict

✉ Liang Tian
tl19852l2@sjtu.edu.cn; sjtu_tl@126.com

[1] Shijiazhuang Tiedao University, Shijiazhuang 050043, China

[2] School of Naval Architecture, Ocean and Civil Engineering, Shanghai Jiaotong University, Shanghai 200240, China

[3] CRCC Bridge Engineering Bureau Group Co., Ltd, Tianjin 300300, China

thermo-mechanical behavior with acceptable accuracy. Deng et al. (2007a, b, 2008, 2010) conducted a series of numerical and experimental studies to reveal the formation mechanism and distributions of welding deformations for different welded structures with T-joint. Perić et al. (2014) presented a numerical and experimental study of residual stresses and distortions induced by the T-joint welding process, and the developed shell/solid element model can improve both the computational efficiency and accuracy. Besides, Perić et al. (2016) also proposed an engineering approach for T-joint fillet welding simulation using simplified material properties. Wang et al. (2013a, 2016, 2017) proposed a kind of elastic FE computational approach with inherent deformation and interface element to predict and mitigate the welding distortions in the production of complex welded structures. Atabaki et al. (2014) conducted experimental and numerical investigations for hybrid laser arc welding of aluminum alloys in the thick T-joint configuration, and experiments verified the numerical simulations. Chen et al. (2015) and Shen and Chen (2014) proposed a hybrid model with shell and solid elements, which was used to calculate the welding-induced distortions of fillet-welded joint and stiffened plate structure, the research results show that the hybrid model can ensure calculation accuracy and save computing time. Fu et al. (2016) developed a sequentially coupled thermo-mechanical finite element model to investigate the effects of welding sequence on the distortions and residual stresses in T-joint welds. Liang et al. (2016) proposed an improved inverse analysis method with the help of cutting technique to obtain the inherent deformations in an Al-alloy thin-plate joint that buckling distortion occurs. Ma et al. (2015) investigated the effect of jig constraint position and pitch on welding deformations for bead-on-plate welding, and it was observed that the angular distortions could be greatly reduced by jig constraint. Chen and Soares (2016) established a nonlinear thermo-elastic–plastic model to study the effects of plate configurations on the weld induced deformations and compressive ultimate strength of fillet-welded plates. Vetriselvan et al. (2017) studied the effect of welding sequences and directions on the out-of-plane distortion in the tube to pipe T-joints using finite element method (FEM), it was shown that the welding direction plays a significant role in minimizing the out-of-plane distortions of the T-joints. In addition to the above researches, there are still many scholars that have investigated the production mechanisms, influencing factors, mitigation practices and prevention strategies for welding deformations of different welded structures containing various welding joints using different methods.

A literature survey shows that the finite element method and experimental measurement have been widely used to investigate the welding-induced deformations of different welded structures (Jung and Tsai 2004; Vakili-Tahami and Ziaei-Asl 2013; Deng et al. 2007a, b, 2008, 2010; Perić et al. 2014, 2016; Wang et al. 2013a, 2016, 2017; Atabaki et al. 2014; Chen et al. 2015; Shen and Chen 2014; Fu et al. 2016; Liang et al. 2016; Ma et al. 2015; Chen and Soares 2016; Vetriselvan et al. 2017). However, these two kinds of methods inevitably have some inherent disadvantages, e.g., the welding simulation using thermo-elastic–plastic finite element method is time-consuming and requires a considerable computing power due to the inherent strong nonlinearity of welding, which makes it difficult to practical application for large-complex engineering structures. Experimental research needs to take up a considerable amount of manpower and material resources. In spite of this, it is necessary and vital to predicting the welding deformations before welding under certain technological conditions, which is helpful to make reasonable design procedures to compensate for welding deformations. Therefore, developing a reliable model that can predict the welding deformations efficiently and accurately under certain process parameters is of great necessity. The development of evolutionary algorithms and intelligent techniques provide an alternative to achieve the idea that is the basis of this research. In this study, the inherent deformations of T-joint fillet weld were predicted by using support vector machine with parameters optimized by the genetic algorithm.

During the past decades, intelligent modeling technologies have been widely used in different aspects of welding, including welding distortions, weld geometry, residual stresses, stress concentration factor (SCF), parameters optimization, mechanical properties, defect diagnosis, etc. A large number of literature surveys were carried out on the several aspects mentioned above.

In the aspect of welding deformations, Sudhakaran et al. (2012) investigated the optimization of process parameters using particle swarm optimization (PSO) to minimize angular distortions in 202-grade stainless steel gas tungsten arc welded plates. Choobi et al. (2012) applied BP neural network to predict the welding-induced angular distortions in thin butt-welded plates, the training data for the model were obtained from a series of finite element simulations with a wide range of plate dimensions. Tian et al. (2014) presented a BP neural network model for the prediction of angular distortions and transverse shrinkages generated in GTA bead-on-plate welding process, the BPN model was established based on finite element simulations, and welding experiments verified the prediction performance. In order to reduce the weld induced distortions of the final welded structure, Islam et al. (2015) developed a sequentially integrated FEM–RSM–GA model to determine the optimal process parameters of lap joint fillet weld, then the effectiveness of the proposed methodology was verified by the optimization results.

In terms of weld geometry characterization, Nagesh and Datta (2002) applied BP neural networks to associate the welding process parameters with the features of the weld bead geometry and penetration in shielded metal-arc welding without considering the structure of the neural network. Kanti and Rao (2008) developed a BP neural network model for the prediction of weld bead geometry in pulsed GMA welding based on experimental data; the proposed model produced good results compared with experimental results. Dey et al. (2009) carried out bead-on-plate welding on austenitic stainless steel plates, used a genetic algorithm (GA) to determine optimal weld-bead geometry and generated preferred process parameters. Huang and Kovacevic (2011) used the acoustic signatures acquired during the laser welding process of high strength steels to characterize the depth of weld penetration, by using a neural network and multiple regression analysis. The results show that the acoustic singles processed by the noise reduction method can predict the depth of weld penetration well under different laser welding parameters. In order to improve the quality of a weld joint, Katherasan et al. (2014) presented the simulation of weld bead geometry in flux cored arc welding. A relationship between the input and output parameters was established by an artificial neural network (ANN), and the optimal process parameters were determined using particle swarm optimization (PSO) algorithm, resulting in the most favorable weld geometry. Sathiya et al. (2012) investigated the relationship between the laser welding input parameters and the three responses such as depth of penetration, bead width and tensile strength of the laser-welded butt joints based on ANN models, and the ANN models were used to optimize the process parameters using a genetic algorithm (GA). Zhang et al. (2015) established a BP neural network optimized by the genetic algorithm to model the relationship between welding appearances and the characteristics of the molten-pool-shadows, the work provided an effective way to predict the weld appearances and assess the welding quality in real-time. A knowledge-based system was established by Jha et al. (2014) to model the bead-on-plate welding of zircaloy-4 plates, in which the input parameters were accelerating voltage, beam current and weld speed, and the output responses were bead width, depth of penetration and micro-hardness. Back-propagation neural network (BPNN), genetic algorithm (GA) and particle swarm optimization (PSO) algorithm were applied to the establishment of this model. Studies have shown that the neural network-based approaches can effectively model this welding process in both forward and reverse directions. Wu et al. (2017) proposed a novel hybrid approach based on particle swarm optimization (PSO) and adaptive-network-based fuzzy inference system (ANFIS) to investigate the relationships between weld joint penetration and keyhole characteristics. Lin (2012) presented an integrated approach using the Taguchi method (TM), grey relational analysis (GRA) and a neural network (NN) to optimize the weld bead geometry in a novel gas metal arc (GMA) welding process. The optimal parameters of the GMA welding process were determined using a well-trained BPNN model.

In the aspect of residual stresses prediction and SCF calculation, Ahmadzadeh et al. (2012) applied the back-propagation neural network to predict the maximum residual stress produced in gas metal arc welding process. Dhas and Kumanan (2016) established a fuzzy SVR model to predict the residual welding stress, and the research results demonstrated that the developed model was superior in terms of computational efficiency and accuracy. Man et al. (2008) presented an SVR method to predict the residual stress for dissimilar metal welding under various welding conditions, and the results show that the SVR models can be used to evaluate the integrity of dissimilar metal welding zones. Similarly, Koo et al. (2017) also studied the distribution of the residual stress in welding of dissimilar metals using a cascaded support vector regression (CSVR) model. Mathew et al. (2017) developed an artificial neural network model to characterize the residual stress profiles of girth welded austenitic stainless steel pipes, and the neural network predictions were validated by experimental measurements. Dabiri et al. (2017) investigated the stress concentration factor in non-load carrying T-welded joints using artificial neural network (ANN) and genetic algorithm (GA) considering different geometrical parameters and loading cases, the ANN model was utilized to evaluate data from the finite element analysis, and optimal combination of variables for T-welded joints was obtained by the GA.

In terms of process parameters optimization, Satpathy et al. (2015) studied the optimal combinations of process parameters for ultrasonic metal welding on dissimilar sheets by using fuzzy logic and genetic algorithm (GA) approach. Tarng et al. (1999) applied neural networks and simulated annealing (SA) algorithm to model and optimize the gas tungsten arc welding (GTAW) process. The relationships between welding process parameters and weld pool features were established by neural networks. An SA optimization algorithm was then used to search for the welding process parameters with optimal weld pool features. Gao et al. (2016) introduced an integrated optimization approach combining Kriging model and GA for the optimization of hybrid fiber laser-arc butt welding parameters. The proposed hybrid technique produced optimum values that were in good agreement with experimental results. For resistance spot welding, Pashazadeh et al. (2016) established a hybrid model consisting of artificial neural networks and multi-objective genetic algorithm to specify the optimized process parameters, including the welding time, the welding current, and the welding pressure. The optimum values of the three welding parameters can be used to achieve the best weld nugget sizes.

In the prediction of mechanical properties of welded joints, Okuyucu et al. (2007) developed an artificial neural network (ANN) model to predict the mechanical properties of welded Al plates as a function of different friction stir welding parameters including weld speed and tool rotation speed, and the anticipated results were in good agreement with measured data. Ates (2007) presented a novel technique based on artificial neural networks to predict the mechanical properties of welded joints, the outcomes of the ANN model were in good agreement with the measured data. Pal et al. (2008) established a multilayer neural network model to predict the ultimate tensile stress of welded plates using arc signals as input variables, the prediction performance of ANN model is better than that of multiple regression analysis. Ghetiya and Patel (2014) employed an ANN model to predict the tensile strength of the FSW joint, and concluded that the developed ANN model provided an effective method for calculating tensile strength under given process parameters. Chaki et al. (2015) applied artificial neural network (ANN), genetic algorithm (GA), simulated annealing (SA) and Quasi-Newton line search techniques to develop the integrated soft computing based models such as ANN–GA, ANN–SA and ANN–Quasi Newton for prediction and optimization of welding strength for hybrid CO_2 laser-MIG welded joints. Taking tool rotary speed and welding speed as inputs, Teimouri and Baseri (2015) developed an effective, intelligent fuzzy system for prediction of tensile strength, elongation and hardness of friction stir welding (FSW) aluminum alloy joint. The model consists of two main approaches, namely artificial bee colony algorithm (ABC) and imperialistic competitive algorithm (ICA), which are respectively used to optimize the fuzzy model and determine appropriate inputs. The results showed that the combination of the modified fuzzy network with ICA is a suitable tool for forward and backward prediction of the FSW process. Dewan et al. (2016) established an optimized adaptive neuro-fuzzy inference system (ANFIS) model to predict tensile strength of FSW joints, by comparing ANFIS and ANN predicted results, it was found that the ANFIS models have a better performance than ANN.

In the aspect of welding quality assessment and defect diagnosis, Baraka et al. (2015) presented a generic data-driven model to predict in real-time the quality of steel FSW based on computational intelligence, and simulation results demonstrated the effectiveness of the proposed approach. He and Li (2016) put forward a method combining local mean decomposition (LMD) and support vector machine (SVM) to estimate the welding quality quantitatively. Experimental results were provided to confirm that this approach has an advantage in evaluating the quality of welding formation. Das et al. (2016) proposed a practical method combining wavelet packet and Hilbert-Huang transform to identify the internal defects in friction stir welding process, and then developed an SVR-based model with parameters optimized by grid search method to estimate ultimate tensile strength of the welded samples. Huang et al. (2017) established an improved support vector machine (SVM) model based on genetic algorithm (GA) to realize porosity defect detection and defect diagnosis in the TIG welding process of aluminum alloys. Ai et al. (2016) proposed a defect-reducing optimization model to reduce welding defects for laser butt welding of dissimilar materials, and the particle swarm optimization and back propagation neural network (PSO–BPNN) was utilized to establish the optimization model. Though many researchers have attempted to use intelligent modeling technologies to study various applications in the welding area just as mentioned in the literature above (Sudhakaran et al. 2012; Choobi et al. 2012; Tian et al. 2014; Islam et al. 2015; Nagesh and Datta 2002; Kanti and Rao 2008; Dey et al. 2009; Huang and Kovacevic 2011; Katherasan et al. 2014; Sathiya et al. 2012; Zhang et al. 2015; Jha et al. 2014; Wu et al. 2017; Lin 2012; Ahmadzadeh et al. 2012; Dhas and Kumanan 2016; Man et al. 2008; Koo et al. 2017; Mathew et al. 2017; Dabiri et al. 2017; Satpathy et al. 2015; Tarng et al. 1999; Gao et al. 2016; Pashazadeh et al. 2016; Okuyucu et al. 2007; Ates 2007; Pal et al. 2008; Ghetiya and Patel 2014; Chaki et al. 2015; Teimouri and Baseri 2015; Dewan et al. 2016; Baraka et al. 2015; He and Li 2016; Das et al. 2016; Huang et al. 2017; Ai et al. 2016), the paper on the prediction of inherent deformations using soft computing techniques such as support vector machine (SVM) and genetic algorithm (GA) is scarce in T-joint fillet welding to author's knowledge.

This paper presents the research results of an investigation concerning the relationship between the welding parameters (e.g., welding speed, voltage, current and plate thickness) and the longitudinal and transverse inherent deformations for T-joint fillet welding of SM490A low-carbon steel. A 3D thermal–elastic–plastic finite element (**TEP FE**) model was proposed to simulate the T-joint fillet welding process. Several fillet welding experiments were performed to validate the proposed finite element model. The SVM-based model with parameters optimized by the GA was developed to predict the longitudinal and transverse inherent deformations by using the informative data obtained from the numerical experiments. The comparison between the predicted results by the SVM model and the calculated results obtained from the numerical computations demonstrates that a good agreement has been achieved. The research shows that the integrated model with SVM and GA proposed in this paper can predict both longitudinal and transverse inherent deformations conveniently and accurately for the T-joint fillet welding within a certain range of welding parameters.

The T-joint fillet welding experiment

Materials and specimen

The material used in this experiment is low alloy high-tensile steel named SM490A, which is widely used in industrial

Table 1 Chemical compositions and mechanical properties of SM490A

Chemical composition (mass%)						Mechanical properties		
C	Mn	P	S	Si	Al	Yield strength R_e/MPa	Tensile strength R_m/MPa	Elongation A(%)
0.12	1.06	≤ 0.02	0.006	0.01	0.032	≥ 325	537	≥ 17

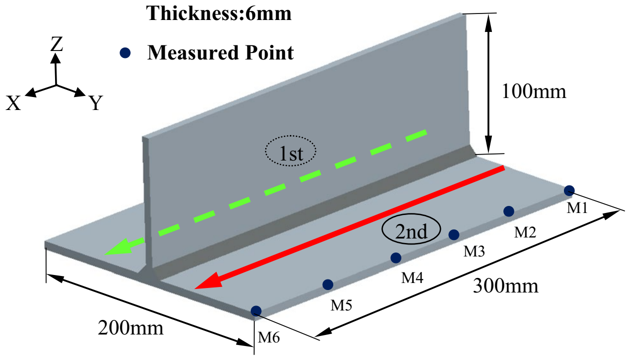

Fig. 1 The fillet welded joint experiment and measured points

Table 2 Welding conditions of fillet welded joint

Weld pass	Welding current I/A	Arc voltage U/V	Welding speed v/(mm/s)	Efficiency
2	170	24	4.3	0.7–0.8

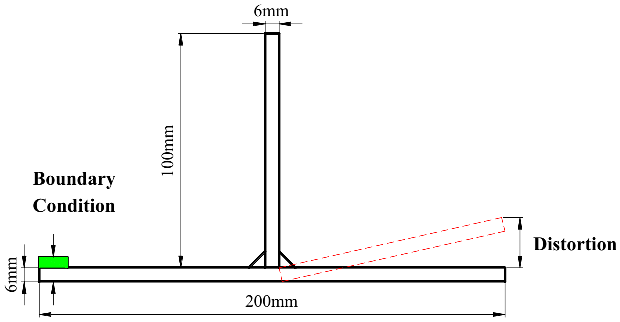

Fig. 2 Boundary condition of the fillet welded joint used in the experiment

applications, especially in shipbuilding, due to its superior performance (Kang et al. 2009; Deng et al. 2015). In particular, SM490A is an important type of structural steel that forms the hull structure. The choice of SM490A as a research material can provide more valuable information for the assessment of inherent deformations of welded joints in the ship and marine structures. The chemical components and mechanical properties of SM490A are shown in Table 1. The geometry and dimensions of the experimental specimen are illustrated in Fig. 1. In this specimen, the length and thickness of the plates are 300 mm and 6 mm, respectively; the breadth of the flange is 200 mm; the height of the web is 100 mm. Both the flange and web were cleaned with a fresh stainless steel wire brush, followed by acetone swabbing before T-joint fillet welding.

Welding experiment and measurement

Hudong–Zhonghua Shipbuilding Group carried out a series of welding experimental researches on typical marine joints, including T-type joints. In this paper, a similar T-joint fillet welding experiment was conducted to measure the angular distortions in order to provide an experimental verification for the finite element model thus developed. The web and flange were tack welded at first, then welded by a single-sided CO_2 gas arc welding process. The welding sequence and direction are shown in Fig. 1. The final welding was conducted using a welding robot with the torch angle at 45°. Table 2 shows the welding conditions, and the same welding conditions are applied to these two welds. The clamping was applied along one side of the flange, and the other side was free during a welding process, just as shown in Fig. 2. The angular distortions at six points along the free side of the flange as shown in Fig. 1 were measured after the welding specimen was completely cooled. The angular distortions of the six measured points are shown in Table 3. These measured data were used to verify the finite element model as developed in the following section. The weld zone of this joint was cut by using a wire electrical discharge machining (WEDM) from the middle of the specimen, then the weld cross section after grinding and polishing is shown in Fig. 3.

Evaluation of inherent deformation for T-joint fillet weld

Theories and methods employed in evaluating the inherent deformations of T-joint fillet weld applied in this research are presented in the following.

Brief review of inherent deformation theory

In theory, the Thermal–Elastic–Plastic Finite Element (**TEP FE**) method can be used to analyze the whole welding process for any complex welding structures. However, the **TEP**

Table 3 The angular distortions of measured points

Measuring points	M1	M2	M3	M4	M5	M6
Angular distortion (mm)	2.55	2.82	2.91	3.34	3.22	3.18

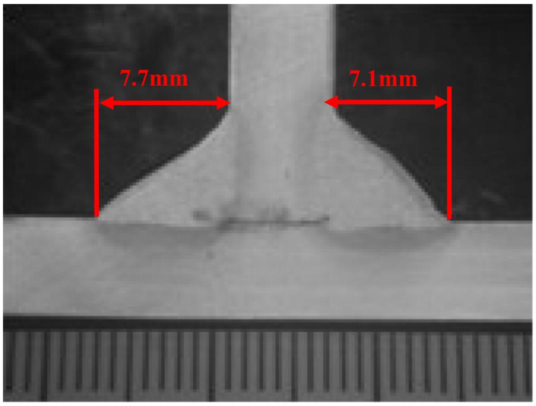

Fig. 3 Cross section of the fillet welded joint showing fillet size

FE analysis requires a very long computing time due to the nonlinear characteristics of the welding, which limits its practical applications in the large-scale and complex engineering structures. In view of this, the Japanese scholars (Ueda et al. 1995, 2012; Ueda and Yuan 1993; Ueda and Ma 1994) put forward the concept of inherent strain in order to predict the welding induced deformations and stresses more conveniently and effectively. According to inherent strain theory, the inherent strain is considered to be the cause of welding residual stresses and welding distortions. Generally speaking, the total strain ε^{total} can be divided into the strain components given by Eq. (1), namely, elastic strain $\varepsilon^{elastic}$, thermal strain $\varepsilon^{thermal}$, plastic strain $\varepsilon^{plastic}$, creep strain ε^{creep} and that produced through phase transformation ε^{phase}.

$$\varepsilon^{total} = \varepsilon^{elastic} + \varepsilon^{thermal} + \varepsilon^{plastic} + \varepsilon^{creep} + \varepsilon^{phase} \tag{1}$$

The total strain can be rearranged as a summation of the elastic strain and the inherent strain ε^*. The inherent strain ε^* can be defined as the summation of plastic, thermal, creep strains and strain caused by the phase transformation as given by Eq. (2). Usually, the thermal strain component will offset to zero after undergoing a heating–cooling cycle of welding. The creep strain and strain caused by solid-state phase transformation are negligible for welded joints made of carbon steel (Deng and Murakawa 2008). Then the inherent strain can be considered as the plastic strain remaining in the weld zone as given by Eq. (3). The following investigation is based on this hypothesis for the sake of simplicity.

$$\varepsilon^{total} - \varepsilon^{elastic} = \varepsilon^{thermal} + \varepsilon^{plastic} + \varepsilon^{creep} + \varepsilon^{phase} = \varepsilon^* \tag{2}$$

$$\varepsilon^* = \varepsilon^{total} - \varepsilon^{elastic} = \varepsilon^{plastic} \tag{3}$$

The elastic FE analysis with employing inherent strain directly to predict residual stresses and welding distortions requires a fine enough FE mesh near the welding line, which is considered inconvenient from a practical viewpoint. Therefore, the inherent deformation is later proposed to avoid such a fine mesh, which depends on the hypothesis that a welded joint in plate structure has an inherent amount of local deformation on every cross section normal to the weld line (Wang et al. 2009, 2014). Similar to the inherent strain, the inherent deformation mostly depends on the joint and welding parameters such as configuration, material properties, plate thickness and welding heat input (Ueda et al. 2012). The distribution of inherent deformation is fairly uniform in the middle part of the welded joint when the welding line is long enough. Therefore, the components of inherent distortion can be approximated as constant values along the welding line if the edge effect can be ignored. As an initial load applied to the elastic FE model, the inherent deformation method can be used to efficiently predict the welding deformations without significant loss of computational accuracy. Accordingly, one prerequisite for applying this method is to determine the inherent deformations of each joint in the welded structures. Due to the importance of inherent deformation in predicting welding induced distortions, so the focus of this paper is to study how to obtain the inherent deformations more accurately and quickly using the evolutionary algorithms and intelligent techniques.

The basic components of inherent deformation can be divided into four types, including longitudinal shrinkage, transverse shrinkage, longitudinal bending and transverse bending (angular distortion), which are defined as the integration of inherent strain distributed on the cross section normal to the welding line according to Eq. (4).

$$\begin{cases} \delta_x^* = \dfrac{1}{h} \iint \varepsilon_x^* dydz \\ \delta_y^* = \dfrac{1}{h} \iint \varepsilon_y^* dydz \\ \theta_x^* = \dfrac{12}{h^3} \iint \varepsilon_x^* (z - h/2) dydz \\ \theta_y^* = \dfrac{12}{h^3} \iint \varepsilon_y^* (z - h/2) dydz \end{cases} \tag{4}$$

where δ_x^* and δ_y^* denote the inherent shrinkage in the longitudinal and the transverse directions; θ_x^* and θ_y^* are the inherent longitudinal bending, inherent transverse bending; ε_x^* and ε_y^* are the longitudinal plastic strain (parallel to welding line) and transverse plastic strain (normal to welding line) near the weld zone; h is the thickness of the welded joint; and x, y, z are the coordinates in welding direction, transverse direction and thickness direction, respectively.

There are three types of methods that can evaluate the inherent deformation, such as formula method, integration method, and displacement method. Among these three methods, it is convenient and efficient to obtain the longitudinal inherent deformation by the displacement method, without a significant loss of calculation accuracy. Therefore, the direct approach based on displacement was adopted in this paper, and the other two calculation methods can be referred to the literature (Wang 2012). As can be seen from Fig. 4, the middle part of the longitudinal displacement curve is almost linear with a constant slope. Since the slope of the longitudinal displacement in the middle part is equal to the longitudinal strain ε_L in welding direction, thus, the longitudinal inherent shrinkage δ_L^* can be obtained from the longitudinal strain ε_L and the tendon force F_{tendon} by the following equation (Wang et al. 2013b):

$$\varepsilon_L = \frac{F_{tendon}}{AE} = \frac{Eh\delta_L^*}{BhE} = \frac{\delta_L^*}{B} \tag{5}$$

$$\delta_L^* = B\varepsilon_L \tag{6}$$

where A, B and h are the cross-sectional area, plate width and plate thickness, respectively.

Since the deformation constraint in transverse direction is smaller than that in longitudinal direction, the transverse inherent shrinkage can be obtained by directly measuring the transverse displacements of the sample points along the welding path.

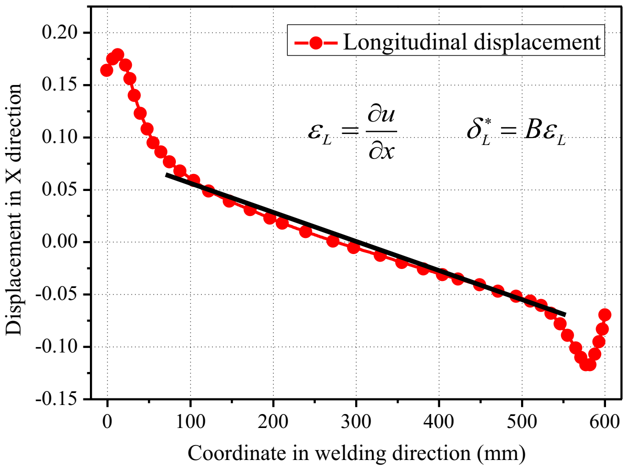

Fig. 4 Distribution of longitudinal displacement along welding line

FE analysis model

The **TEP FE** analysis is the basis for evaluating the inherent deformations using the displacement method mentioned above, the implementation procedures of **TEP FE** analysis for T-joint were elaborated in the following, and then the developed **TEP FE** model was verified by experimental data.

Establishment of the finite element model

In this study, the T-joint fillet welding process was simulated using an uncoupled thermo-mechanical FE formulation based on ABAQUS code. The numerical simulation was carried out in two steps. First of all, the temperature distribution and its history were calculated by a nonlinear transient thermal analysis. The volumetric heat source model was used to solve the heat conduction problem for fusion welding. Secondly, the subsequent mechanical analysis was performed with the temperature history obtained from the previous step as an initial thermal load.

In thermal and mechanical analysis, a bilinear kinematic hardening model (BKIN) was adopted to model the constitutive properties of the selected material. The temperature-dependent thermo-physical and mechanical properties of the base metal (SM490A steel) were taken into account in the numerical model, as shown in Figs. 5 and 6, respectively (Deng et al. 2015). A solid FE model of the T-joint with the same dimensions as the welded specimen was established, and the cross-section of each weld was similar to that of the corresponding actual weld bead. The meshes of the model are shown in Fig. 7, which consist of 12,803 nodes and 10,020 elements. In order to balance the computing time and calculation accuracy, finer meshes were adopted in the weld

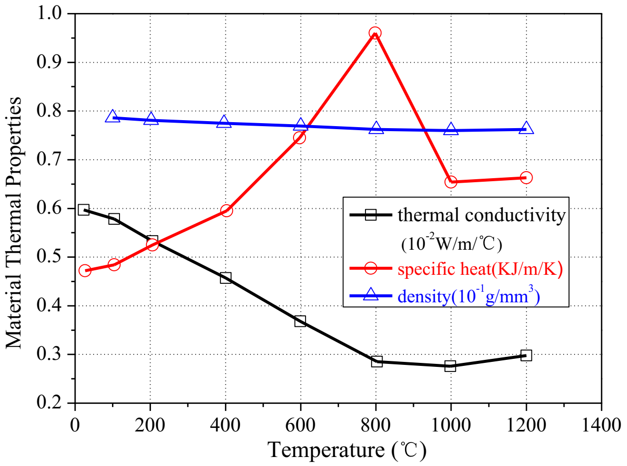

Fig. 5 Temperature-dependent thermal physical properties of SM490A

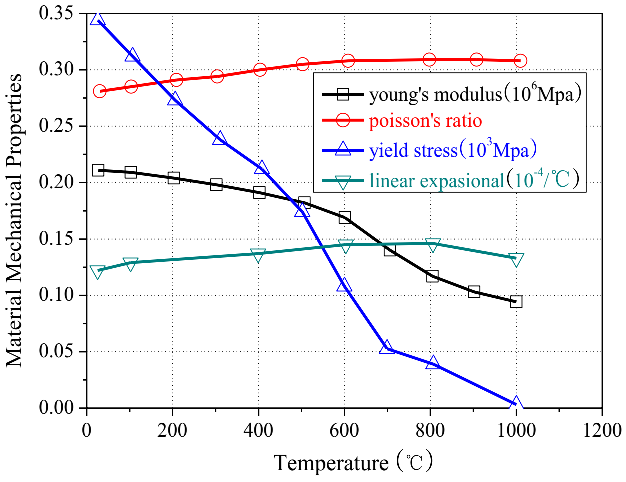

Fig. 6 Temperature-dependent mechanical properties of SM490A

zone and its vicinity, while relatively coarser grids were used in the region away from the welding line. The minimum element in the weld zone is 1 mm × 1 mm × 1.5 mm. The element types adopted in the model are DC3D8 and C3D8I, which are used for thermal and mechanical analysis, respectively.

Thermal analysis

The purpose of the transient thermal analysis is to obtain the temperature field history during the T-joint fillet welding process, which can be used as a thermal load in the subsequent mechanical analysis. In the calculation of the temperature field, the moving heat source is treated as a volumetric heat flux with uniform density. Each weld pass is divided into a number of small parts with equal length, and each mesh block is sequentially heated to simulate the moving arc. The cross area of a heat source in the FE model is roughly equal to that of the weld bead measured by experiment. The heat input of each weld pass can be calculated using the welding parameters as shown in Table 2, and the volumetric heat flux (q_V) can be expressed using the following equation (Deng et al. 2011):

$$q_V = \frac{\eta UI}{V_H} = \frac{Q_{net} v_w}{V_H} \tag{7}$$

where U is the arc voltage, I is the welding current, V_H is the volume of heat source, Q_{net} is the nominal heat input, v_w is the welding speed of each weld pass, and η represents the arc efficiency factor, which is assumed to be 0.7–0.8 for CO_2 gas metal arc welding (Radaj 1992).

The number of divisions in longitudinal direction of the FE model is 30, so the heating time (t_h) for each mesh block is determined by the following equation:

$$t_h = \frac{L_w}{30 v_w} \tag{8}$$

where L_w is the total length of weld seam (300 mm), as shown in Fig. 1. In this simulation, the welding parameters, such as arc voltage, current and welding speed, are identical to those used in the experiment.

The volumetric flux for the moving welding arc is modeled by a user subroutine DFLUX in ABAQUS developed by FORTRAN programming. The peak temperature of the weld pool can be controlled within a reasonable range (approximately 1700 ± 150 °C) through using the body heat source with uniform density. Then the suitable body heat source model can be derived and used in the thermal analysis of the T-joint fillet welding. Figure 8 shows the transient temperature distribution of the FE model when the welding time $t_w = 45.6$ s, that is, the first weld bead is being welded. The maximum temperature of the weld pool can be up to 1631 °C from Fig. 8.

Besides considering the moving heat source, heat losses from the welded surface due to convection and radiation are also taken into account in the FE model of the fillet welded joint. Radiation losses are dominant near and in the weld zone for higher temperatures, while convection losses for

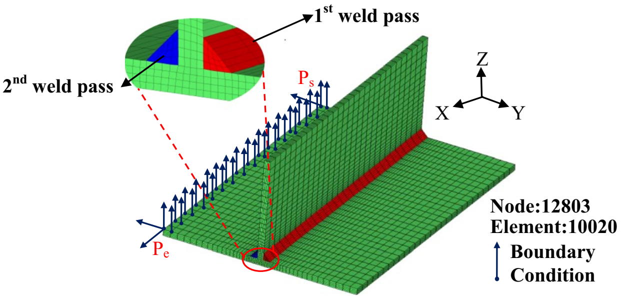

Fig. 7 FE model and boundary conditions of the fillet welded joint

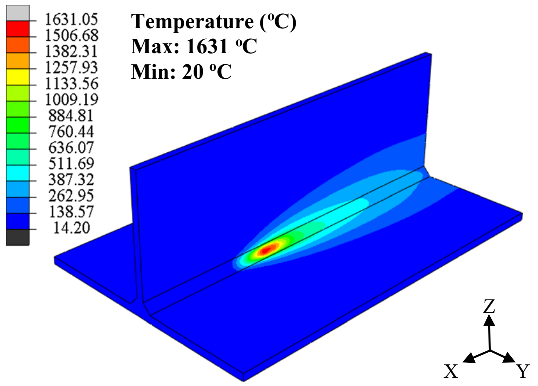

Fig. 8 Transient temperature distribution during the fillet welding

lower temperature are the dominant heat loss away from the weld zone. Considering the effects of radiation and convection on heat loss, the total temperature-dependent film coefficient is given by Eq. (9) (Brickstad and Josefson 1998):

$$H = \begin{cases} 0.668 \cdot T \times 10^{-7}\left(\mathrm{W}/\mathrm{mm}^2\right) & 0 < T < 500\,^{\circ}\mathrm{C} \\ (0.231 \cdot T - 82.1) \times 10^{-6}\left(\mathrm{W}/\mathrm{mm}^2\right) & T > 500\,^{\circ}\mathrm{C} \end{cases} \tag{9}$$

where T is the transient temperature during welding simulation.

The combined thermal boundary conditions are modeled by a user subroutine program developed with FORTRAN, which is then applied to all free surfaces of the welded joint. In order to account for the heat transfer due to fluid flow in the weld pool, an artificially increased thermal conductivity is assumed for temperatures above the melting point. Similarly, the latent heat released during solidification of the weld pool is also simulated by increasing the specific heat at the melting temperature. Figure 5 shows the temperature-dependent thermal physical properties of SM490A steel used in the thermal analysis.

Mechanical analysis and experimental verification

The mechanical analysis is carried out by using the temperature results calculated in the above thermal analysis as the input data. The same finite element models used in the thermal analysis are applied to the mechanical analysis. The only difference is the element type and boundary conditions. The element type is changed to C3D8I, and the mechanical boundary conditions are constrained only for preventing rigid body motion as shown in Fig. 7. The nodes located on the edge of the flange are fixed in Z-direction, just like the jig applied to the welding specimen. The point P_s is constrained in the Y and Z direction, and point P_e is constrained in X, Y and Z direction, P_s and P_e in Fig. 7 are the start and end points of the flange edge of the FE model, respectively. In a word, the boundary conditions are the same as those used in the experiment as shown in Fig. 2.

In the mechanical analysis, the elastic stress–strain relationship is modeled using the isotropic Hook's law with temperature-dependent Young's modulus and Poisson's ratio. The thermal strain is calculated using the temperature-dependent coefficient of thermal expansion. For the plastic behavior, a rate-independent plastic model is employed with the Von Mises yield surface as the plasticity criterion. In the present model, the strain hardening is taken into account using the isotropic hardening rule with a bilinear stress–strain curve because material points typically undergo both loading and unloading in the welding process. Meanwhile, the annealing effect is also incorporated into the simulation model, that is, when the temperature of material point is higher than the annealing temperature, the material will lose its hardening memory, and when the temperature of the material point falls below the annealing temperature, the material point recovers its hardening effects again. Similar to thermal analysis, the temperature-dependent mechanical properties of SM490A such as Young's modulus, yield strength, Poisson's ratio, and thermal expansion coefficient are used in the mechanical model, as shown in Fig. 6.

In order to verify the effectiveness of the FE model developed above, a series of T-joint welding experiments have been carried out. The measuring positions in the FE model are the same as those in the T-joint fillet welding experiments performed in "Welding experiment and measurement" section, as shown in Fig. 1. The measuring method for simulative values is also the same as the experimental one. Figure 9 shows the contours of the angular distortion distribution. UZ is the displacement of Z-direction and is chosen to measure the values of angular distortion. As can be seen from Fig. 9, the maximum displacement of UZ is close to 3.34 mm, which is located on the free edge of the flange in the FE model. Six sets of experimental data obtained by experiments are used for comparison with the simulation results. The unconstrained flange edge of the model is taken as the measuring line 1, as shown in Fig. 10. From the figure, it is observed that the simulation results on line 1 are quite close to the experimental measurements. This proves that the developed **TEP FE** model can produce the experimental results with higher accuracy so that it can be used in the following numerical experiments.

Calculation of the inherent deformation

The calculation of the inherent deformations for T-joint is based on the simulation results of the **TEP FE** model developed above. The longitudinal inherent shrinkage of the model is evaluated by the displacement method, which has been discussed in detail in "Brief review of inherent deformation theory" section. Selecting the measuring points close to and away from the welds, and its longitudinal

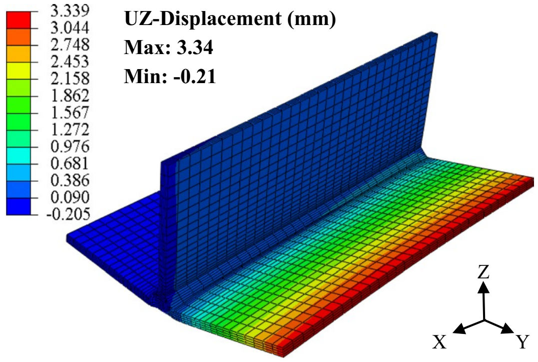

Fig. 9 Z-direction displacement distribution

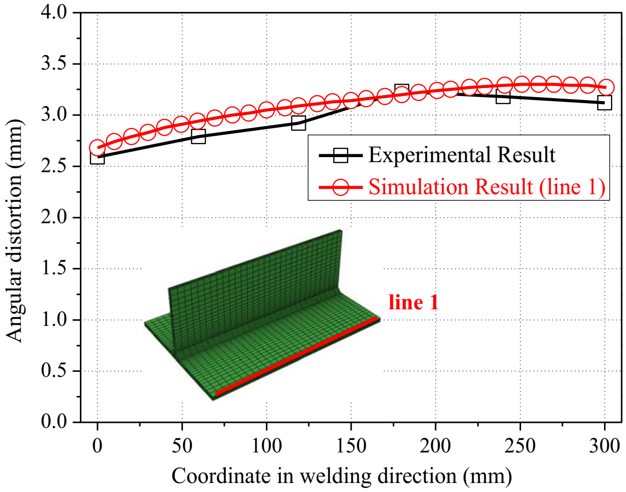

Fig. 10 Comparison between simulation and experimental results of angular distortion

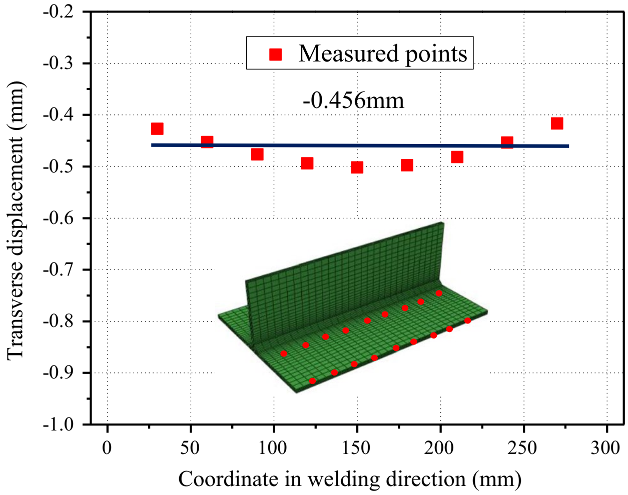

Fig. 12 Distribution of transverse displacement along welding line

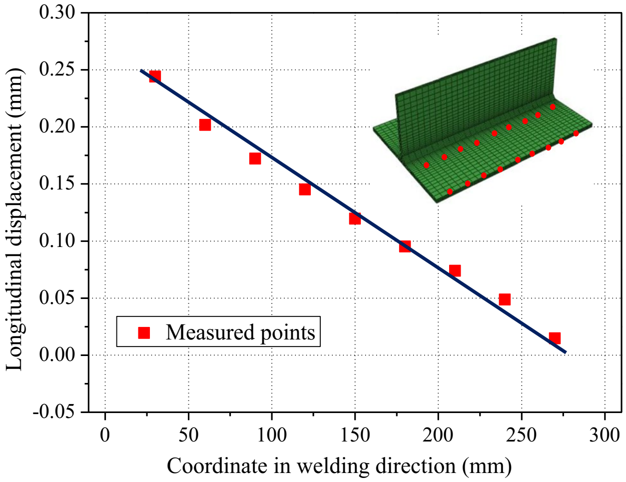

Fig. 11 Distribution of longitudinal displacement along welding line

displacements along the welding line are shown in Fig. 11. According to the definition of the displacement method given by Eqs. 5 and 6, the slope of the longitudinal displacement is equal to the longitudinal strain δ_L. Therefore, the longitudinal inherent shrinkage δ_L^* can be calculated using the measured longitudinal displacement as follows:

$$\delta_L^* = B\varepsilon_L = B\frac{\partial u}{\partial x} = 200 \times \frac{0.0507}{60} = 0.169\,\text{mm} \tag{10}$$

The transverse inherent shrinkage can be obtained by directly measuring the transverse displacements of the measured points along the welding direction. Figure 12 shows the distribution of transverse displacement along the welding line, with an average value of − 0.456 mm. The longitudinal and transverse inherent deformations evaluated by two different methods (displacement method and integration method) are compared in Table 4. As may be seen from this table, the inherent deformations evaluated by displacement method agree well with those evaluated using the integration method. Therefore, this further proves the validity of the **TEP FE** model and the inherent deformation evaluation method discussed above, which can be used to provide reliable input data for the SVM model as developed in the following section.

Table 4 Comparison of estimated longitudinal and transverse inherent shrinkage

Inherent deformations (mm)	Displacement method	Integration method
Longitudinal (mm)	0.169	0.171
Transverse (mm)	0.456	0.535

Proposed SVM model for predicting inherent deformation

The basic theories and methodologies used to establish the SVM-based prediction model for inherent deformation in this research are presented in the following.

Preliminaries of SVM for regression and GA

For the readers' convenience, some background knowledge on the SVM for regression and genetic algorithm (GA) is firstly provided in this section.

SVM for regression estimation

Support vector machine (SVM), originally proposed by Vapnik (1995), is based on the statistic learning theory and structural risk minimization principle (SRM) that pursues minimizing the upper bound on the expected risk. Originally, SVM is developed for pattern recognition problems. Recently, with the introduction of a ε-insensitive loss function, the SVM also has been extended and widely used to perform nonlinear regression estimation, time-series prediction, system nonlinear identification and control. When the SVM is applied to regression problems, it is referred to as support vector regression (SVR). The SVR method has unique theoretical advantages in solving a variety of welding problems such as residual stress, welding deformations and so on.

The primary principle of the SVR method involves nonlinearly converting the initial input data $\mathbf{x}$ into a high dimensional characteristic space and then performing linear regression analysis in the high dimensional characteristic space. This conversion can be accomplished by using various nonlinear mapping. The nonlinear regression problem in the input space is transformed into a linear regression problem in the characteristic space. The SVR model is constructed using N learning data, and the learning data are expressed as $\left\{\left(\mathbf{x}_i, y_i\right)\right\}_{i=1}^{N} \in R^m \times R$, in which $\mathbf{x}_i$ denotes the input data vector and y_i denotes the corresponding output value, from which it learns the input–output relationship. The SVR model can be expressed as follows (Kecman 2001):

$$y = f(x) = \sum_{i=1}^{N} w_i \phi_i(x) + b = \mathbf{W}^T \mathbf{\Phi}(\mathbf{x}) + b \tag{11}$$

where the function $\phi_i(x)$ denotes a nonlinear mapping function from the input space $\mathbf{x}$, $\mathbf{W} = [w_1\ w_2\ \ldots\ w_N]^T$, and $\mathbf{\Phi} = \left[\phi_1\ \phi_2\ \cdots\ \phi_N\right]^T$. The parameters $\mathbf{W}$ and b are the weight of support vectors and bias, respectively, which can be calculated by minimizing a regularized risk function that is expressed as given below (Kecman 2001):

$$R(\mathbf{W}) = \frac{1}{2}\mathbf{W}^T\mathbf{W} + \lambda\left(\sum_{i=1}^{N} \mu_i\left(\xi_i + \xi_i'\right)\right) \tag{12}$$

subject to the following constraints:

$$\begin{cases} y_i - w^T\phi\left(x_i\right) \le \varepsilon + \xi_i,\ i = 1, 2, \cdots, N \\ w^T\phi\left(x_i\right) - y_i \le \varepsilon + \xi_i',\ i = 1, 2, \cdots, N \\ \xi_i,\ \xi_i' \ge 0, i = 1, 2, \cdots, N \end{cases} \tag{13}$$

where λ is a regularization parameter, which represents a balance between the model complexity and the approximation error, an increase of the regularization parameter λ leads to a decrease of approximation error. ε denotes the insensitivity zone, the constants λ and ε are user-specified parameters, which have a significant influence on the prediction accuracy of the model. ξ_i and ξ_i' represents the upper and lower constraints on the outputs of the model.

In order to solve the optimization problem more easily, the Lagrange multiplier technique is applied to solve Eqs. (12) and (13). Finally, the regression function of Eq. (14) can be obtained as follows:

$$y = f(x) = \sum_{i=1}^{N} \left(\alpha_i - \alpha_i^*\right) K\left(x, x_i\right) + b \tag{14}$$

where the coefficients $\alpha_i - \alpha_i^*$ have nonzero values that are solved by a quadratic programming technique, and the corresponding training data vectors are called support vectors. $K(x, x_i)$ is the so-called kernel function. The commonly used kernel functions consist of the linear kernel, sigmoid kernel and the polynomial kernel with different degrees. Generally, the radial basis function (RBF) yields better prediction performance due to its robustness and symmetry properties. Thus, in this study, the developed SVM model is equipped with the RBF as the kernel function defined by Eq. (15).

$$K\left(x_i, x\right) = \exp\left(-\frac{\left(x - x_i\right)^T\left(x - x_i\right)}{2\sigma^2}\right) \tag{15}$$

where σ represents the sharpness of the radial basis kernel function.

Genetic algorithm (GA)

Genetic algorithm (GA) is chosen to optimize the related parameters of the developed SVM model. GA is an intelligent stochastic global search algorithm inspired by natural evolution, which is less susceptible to being stuck at local minima than conventional search methods since GA explores all regions of the solution space using a population of individuals (Mitchell 1996). GA has been applied to many complex optimization problems, especially with multiple objectives due to its superiority compared to traditional optimization methods.

The main operations of GA include selection, crossover, and mutation. Selection is an operation which chooses more fit individuals from the population based on fitness value. The individual chosen in this study is a set of parameters including the regularization parameter λ, the insensitivity zone ε and the sharpness σ of the RBF. The initial population of individuals is generated randomly in the first generation. In each generation, the fitness of every individual in the population is evaluated, and the higher the individual fitness value is, the more likely it is selected. Then, the mutation and crossover are applied to individuals selected to produce the next generation of individuals for fitness evaluation. The new generation is then used for the next iteration of the algorithm. This iteration process terminates until a maximum number of generations has been produced, or a satisfactory fitness level has been reached for the population. Finally, the optimal individual can be obtained by the generational process.

The basic formula of GA is defined as follow:

$$GA = \left(C, E, P_0, N, \varphi, P_c, P_m, T\right) \tag{16}$$

where C is the individual coding method, E is the fitness function of each individual, P_0 is the initial population, N is the population size, φ is the selection operator, P_c is the crossover operator, P_m is the mutation operator, T is the termination condition.

Numerical experiments

The designed SVM model should be trained by a number of samples in order to make it acquire the knowledge inherent in the experimental data. Therefore, obtaining a set of typical sample data on the inherent deformations is a prerequisite for the subsequent training process of the SVM model. The purpose of numerical experiments is to provide the training data for establishing the SVM model as described in "SVM for regression estimation" section. An effective **TEP FE** model of T-joint was developed in "FE analysis model" section, which can produce a set of training data (longitudinal and transverse inherent deformations) under a given range of welding conditions. The numerical experiments were performed based on the **TEP FE** simulations, and the implementation of the inherent deformations was carried out by the method elaborated in "Brief review of inherent deformation theory" section. According to practice and experience, several important welding process parameters affecting the inherent deformations were considered in the numerical experiments, including welding voltage, current, speed and plate thickness.

To save the computing resources and improve the coverage of the samples, the orthogonal experiment was designed to perform the **TEP FE** analyses for the T-joint fillet weld under ABAQUS platform. An orthogonal list with 4 factors and 5 levels was adopted in the design of experiments, which can generate 25 sets of processing parameters, as shown in Table 5. The other 25 sets of processing parameters were generated randomly by MATLAB. Thus, a total of 50 sets of processing parameters were obtained to conduct the numerical experiments, and then 50 training samples on inherent deformations were collected through the above experimental scheme, just as shown in Table 6. Figure 13 shows the distribution of training samples including longitudinal and transverse inherent deformations, which can be used to train the SVM model as developed in the following section.

Establishment of SVM model optimized by the GA

The training samples used to establish the SVM model have been obtained in "Numerical experiments" section. In the following, the implementation processes of the data-based SVM model are presented.

General framework of SVM model

The **TEP FE** simulation and experimental study for the T-joint fillet weld show that the relationship between welding parameters (i.e., welding speed, current, voltage, and plate thickness) and inherent deformations (i.e., longitudinal and transverse inherent deformations) is nonlinear. So it is very difficult to present an explicit mathematical function to describe this nonlinear relationship. Moreover, it is also impractical to use the **TEP FE** method for large-scale and complex welded structures. However, the SVM model provides a potential tool for solving this question due to its many attractive features and good generalization performance. Hence, SVM model is developed to map the complex and highly interactive process parameters, namely, welding speed, current, voltage and plate thickness, to predict the longitudinal and transverse inherent deformations in T-joint fillet welding process. The proposed SVM model mainly consists of three modules, as shown in Fig. 14, which realize the functions of data acquisition, algorithm implementation and prediction and verification for the results, respectively. The implementation of the SVM model is described as follows:

Module 1: Dataset description and preprocessing.

Table 5 Setting of the processing parameters for simulation experiments

Parameters	Notation	Unit	Levels of factors				
			1	2	3	4	5
Welding current	I	A	120	170	220	270	320
Welding voltage	U	V	14	24	34	44	54
Welding speed	S	mm/s	2	4.3	9	14	19
Plate thickness	T	mm	3	6	11	16	21

Table 6 The orthogonal experimental scheme and training samples

Sl. no.	Simulation experiment scheme				Simulation results (inherent deformation)	
	Current (I)/A	Voltage (U)/V	Speed (S)/mm/s	Plate thickness (T)/mm	Longitudinal/(E-02 mm)	Transverse/(E-02 mm)
1	120 (1)	14 (1)	2 (1)	3 (1)	−56.9	−47.4
2	120 (1)	24 (2)	4.3(2)	6 (2)	−12.2	−33.5
3	120 (1)	34 (3)	9 (3)	11 (3)	−8.41	−4.61
4	120 (1)	44 (4)	14 (4)	16 (4)	−4.35	−3.35
5	120 (1)	54 (5)	19 (5)	21 (5)	−2.67	−1.96
6	170 (2)	14 (1)	4.3 (2)	11 (3)	−7.64	−11.7
7	170 (2)	24 (2)	9 (3)	16 (4)	−5.2	−7.06
8	170 (2)	34 (3)	14 (4)	21 (5)	−4.89	−4.65
9	170 (2)	44 (4)	19 (5)	3 (1)	−2.03	−1.2
10	170 (2)	54 (5)	2 (1)	6 (2)	−71.1	−42.6
11	220 (3)	14 (1)	9 (3)	21 (5)	−7.19	−8.66
12	220 (3)	24 (2)	14 (4)	3 (1)	−5.42	−5.07
13	220 (3)	34 (3)	19 (5)	6 (2)	−7.3	−6.7
14	220 (3)	44 (4)	2 (1)	11 (3)	−65.8	−52.3
15	220 (3)	54 (5)	4.3 (2)	16 (4)	−22.3	−45.9
16	270 (4)	14 (1)	14 (4)	6 (2)	−1.31	−1.68
17	270 (4)	24 (2)	19 (5)	11 (3)	−3.05	−4.19
18	270 (4)	34 (3)	2 (1)	16 (4)	−52.7	−48.4
19	270 (4)	44 (4)	4.3 (2)	21 (5)	−15.3	−32.6
20	270 (4)	54 (5)	9 (3)	3 (1)	−32.7	−37.5
21	320 (5)	14 (1)	19 (5)	16 (4)	−2.38	−1.83
22	320 (5)	24 (2)	2 (1)	21 (5)	−42.5	−51.9
23	320 (5)	34 (3)	4.3 (2)	3 (1)	−58.2	−55.5
24	320 (5)	44 (4)	9 (3)	6 (2)	−62.5	−30.9
25	320 (5)	54 (5)	14 (4)	11 (3)	−8.46	−35.6
26	273.1	35.2	2.1	19	−46.3	−62.8
27	279	45.2	15.2	20	−18.7	−23.9
28	157.4	51.4	15.9	12	−6.38	−8.61
29	218	19.2	16.8	14	−3.46	−4.28
30	209.1	36.8	3.4	9	−34.7	−46.3
31	249.3	32.8	8.8	20	−43.6	−57.3
32	261.8	14.5	6.4	10	−8.26	−17.8
33	271.9	27.5	15.6	5	−6.92	−6.75
34	175.2	20.5	9.3	17	−4.18	−3.61
35	255.9	45.8	17.5	10	−9.63	−23.7
36	251	26.5	5.1	7	−75.5	−21.2
37	152.5	35.1	6.5	10	−31.8	−43.7
38	143.8	20.6	4.5	4	−38.3	−21.7
39	219.7	38.1	4.3	5	−55.3	−29.5
40	311.9	24.5	16.8	20	−3.8	−6.17
41	188.1	40.2	11.9	16	−2.5	−2.96
42	237	41.6	11.3	13	−64.3	−45.8
43	164.8	43.9	4.5	4	−25.5	−28.4
44	270.3	32	16.5	7	−6.64	−40.6
45	171	17.4	12.6	10	−5.27	−6.53
46	221.2	23.2	8.0	18	−7.5	−2.24
47	259.8	50.5	10.7	3	−70.5	−53.5
48	298.2	20.1	8.8	4	−41.3	−54.7

Table 6 (continued)

Sl. no.	Simulation experiment scheme				Simulation results (inherent deformation)	
	Current (I)/A	Voltage (U)/V	Speed (S)/mm/s	Plate thickness (T)/mm	Longitudinal/ (E-02 mm)	Transverse/ (E-02 mm)
49	311.9	47	3.3	6	−76.5	−61.5
50	229.4	35.5	6.1	15	−48.5	−36.2

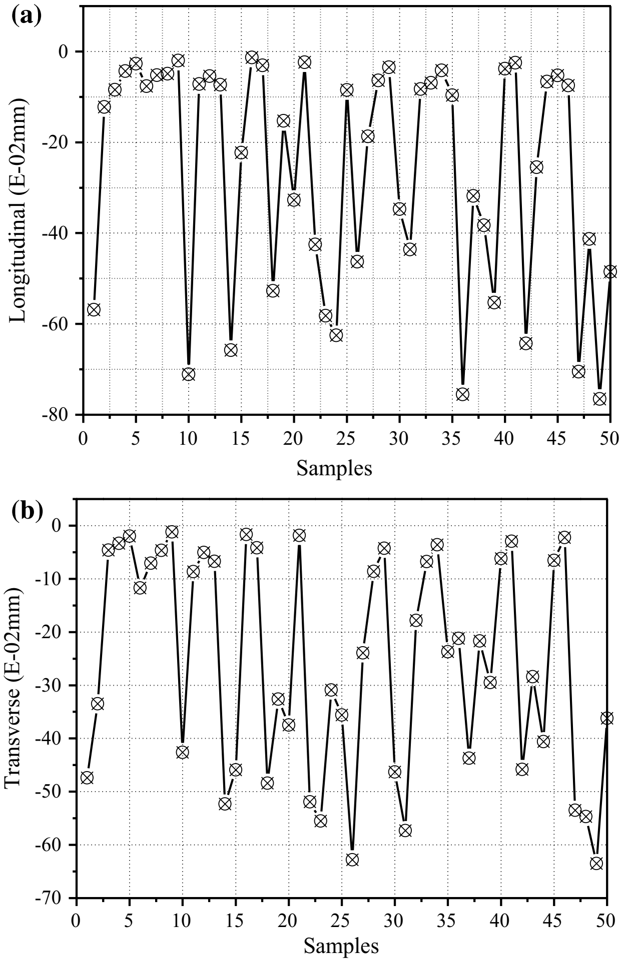

Fig. 13 **a** Longitudinal and **b** transverse inherent deformations distribution of the samples

1. Collecting informative data from the numerical experiments. The input data set of the SVM model is *Input_data* = {*S*, *U*, *I*, *T*}, where *S*, *U*, *I* and *T* are the input variables, which denote the welding speed (mm/s), voltage (V), current (A) and plate thickness (mm), respectively. The output data set is defined as *Output_data* = {*LID*, *TID*}, where *LID* and *TID* are the output variables, which represent the longitudinal and transverse inherent deformations, respectively.
2. Normalize the input/output data. In order to ensure the learning efficiency of the algorithm and prevent a specific factor from dominating the learning process for the developed model, it is necessary to make the sample data dimensionless before applying the SVM model. Normalization processing of the sample data is performed according to the expression $X = (X - \min(X))/(\max(X) \text{ - } \min(X))$, and these data are normalized within the range of [0, 1].
3. The sample data from Table 6 are partitioned into two parts: a training set with 80% of the data and testing set with 20% of the data. The training set and testing set are selected randomly, and the training data does not include the testing data.

Module 2: SVM algorithm implementation.

1. Selecting the RBF kernel as the kernel function of the SVM model.
2. Optimize parameters of SVM using the GA. There are three parameters that need to be optimized, the optimal parameters are obtained by the GA, and then applied to the construction of the SVM model.
3. Estimate the value of the inherent deformations using SVM, compute the Euclidean distance between every output and its corresponding goal, solving the quadratic programming problem.

Module 3: Prediction and verification for the inherent deformations.

1. Output the prediction results from the SVM model, obtain the longitudinal and transverse inherent deformations under a certain range of welding parameters.
2. Evaluate the generalization performance of the developed SVM model using testing data.

SVM parameters optimization using GA

As discussed in "Genetic algorithm (GA)" section above, the generalization performance of the SVM model depends heavily on the three kinds of design parameters, including the regularization parameter λ, the insensitivity zone ε and the sharpness σ of the RBF. Therefore, it is necessary to

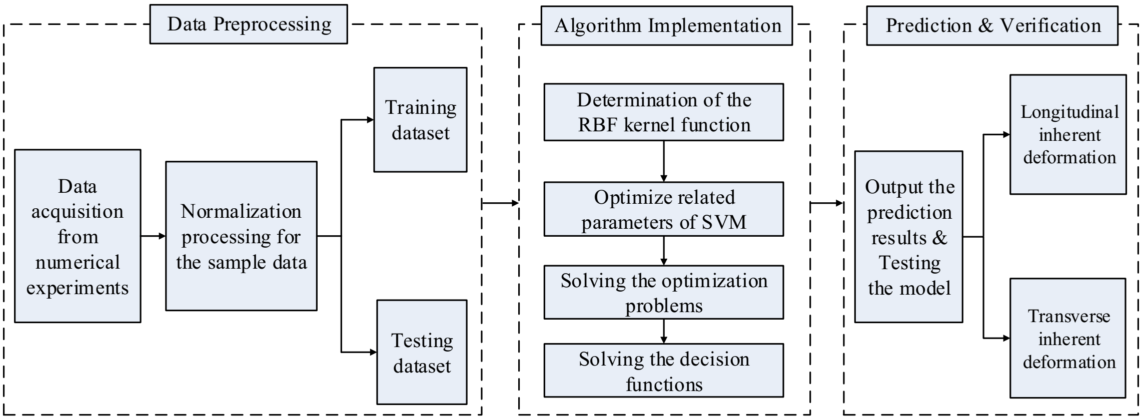

Fig. 14 The main function modules of proposed SVM model

select the optimal SVM parameters in order to eliminate the errors resulting from a random selection of related parameters. GA is employed to optimize the parameters in this study, and then the SVM model can be established and trained by using the optimal parameters. A flow chart of this optimization process is shown in Fig. 15. The main development procedures of GA-based parameters optimization are given as follows:

Step 1: SVM parameters encoding

The encoding scheme maps a possible solution of the optimization problem to a string, also known as a chromosome. The three parameters (λ, ε and σ) to be optimized for the proposed SVM model are encoded in binary form, and their coded bits are n_1, n_2 and n_3, respectively. Then the chromosome X is represented by $X = \{\lambda, \varepsilon, \sigma\}$, which contains all the parameters needed to establish an SVM model. The length of each chromosome is $n_1 + n_2 + n_3$, which represents a candidate solution to the problem.

Step 2: The fitness function

GA requires a fitness function that gives a score to each chromosome (candidate solution) in the current population, which evaluates the extent to which each candidate solution fits the target solution. The selected probability for each chromosome is in proportion to its fitness value, and Roulette Wheel Selection (RWS) is used to perform the selection operation. In this paper, the fitness function is defined as the mean square error (MSE) between the target values and output values, as follows:

Fig. 15 Flow chart of parameters optimization for SVM using the GA

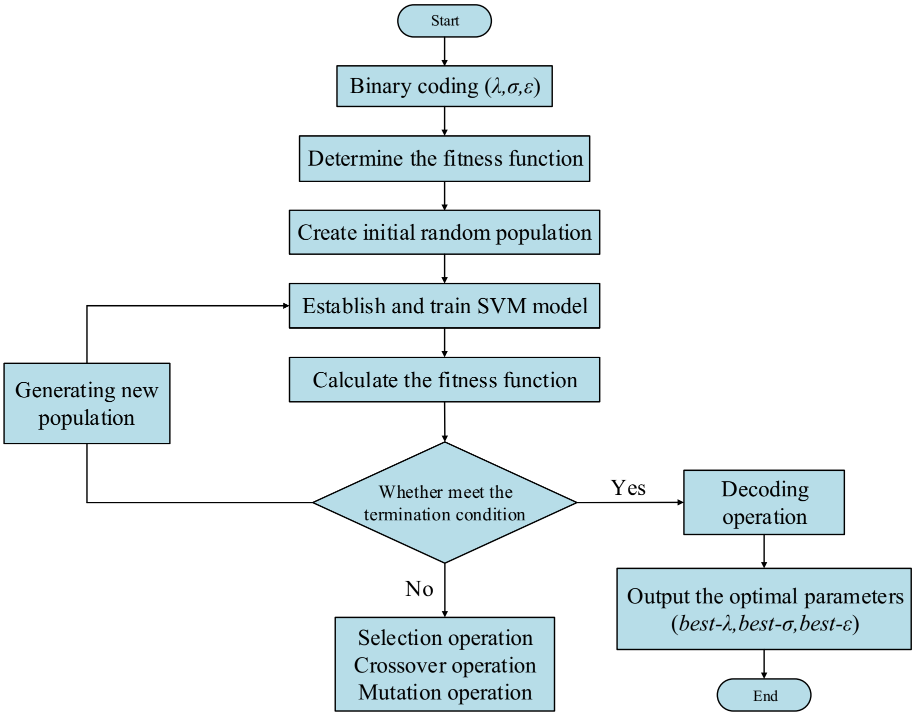

$$f = \frac{\sum_{i=1}^{n} \left[y_i(\lambda, \varepsilon, \sigma) - o_i(\lambda, \varepsilon, \sigma) \right]^2}{n} \tag{17}$$

where y_i denotes the target values of the input data, o_i denotes the output values (predicted values) of the SVM model; n represents the number of training samples.

From the definition of the fitness function, the smaller the fitness value is, the closer the predicted value of the SVM model is to the target value. This indicates that the individuals with smaller fitness value are more likely to be retained. The optimal parameters of the SVM model are the best individual when the evolutionary process terminates.

Step 3: Generating initial population

GA starts with an initial population of coded solutions to the optimization problem. The initial population of chromosomes is generated randomly, which represents the three parameters (λ, ε and σ) to be optimized for the SVM model. The range of values for each parameter in the initial population is given as follows:

The regularization parameter λ: $0 \leqq \lambda \leqq 100$;
The insensitivity zone ε: $0.001 \leqq \varepsilon \leqq 1$;
The RBF parameter σ: $0 \leqq \sigma \leqq 100$.

Step 4: Parameters setting for GA and evolutionary process

The proper selection of GA parameters has a significant influence on its optimization performance. In the present study, the parameters used for GA are set as follows: size of populations $N = 30$; number of stall generations $g = 200$; crossover fraction p = 0.7 and mutation rate $m = 0.1$.

Run the program and GA begins to generational iteration. Then, the fitness value is first calculated and used to evaluate each chromosome in the population. As the generation proceeds, new generations are generated by genetic operations such as selection, crossover, and mutation. The generational process is repeated until the termination is satisfied. The population average fitness curve and the optimal individual fitness curve in the evolutionary process are shown in Fig. 16. After 200 generations of evolution, the optimal parameters of SVM are $\lambda = 6.8070$, $\sigma = 2.5919$ and $\varepsilon = 0.0553$.

The optimal parameters were used to establish the SVM model. After the training process for the SVM model, the bias of the decision function is $b = -0.751590$, the number of support vectors (SVs) is 20. By substituting the known parameters into Eq. (14), then the optimal regression function for the SVM model can be expressed as follows:

$$f(x) = \sum_{i=1}^{20} \left(\alpha_i - \alpha_i^* \right) \exp\left(-2.5919 \left| x - x_i \right|^2 \right) - 0.751590 \tag{18}$$

Based on the above research, the inherent deformations of the T-joint can be approximated by interpolation through solving the optimal support vector regression function. In this way, an SVM model with optimal parameters has been obtained, and its prediction performance will be evaluated in the next section.

Results and discussion

In view of the SVM model optimized by the GA that was developed above, its prediction performances for the inherent deformations were evaluated by the training and testing samples. Meanwhile, a comparison between the optimized and unoptimized SVM models was also made in this section.

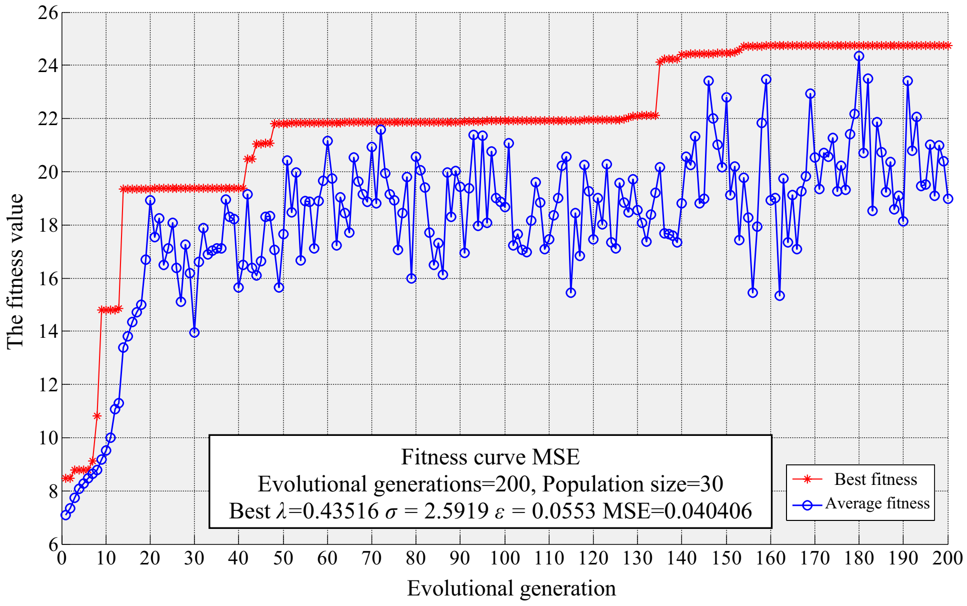

Fig. 16 The fitness curve during SVM parameters optimization process by the GA

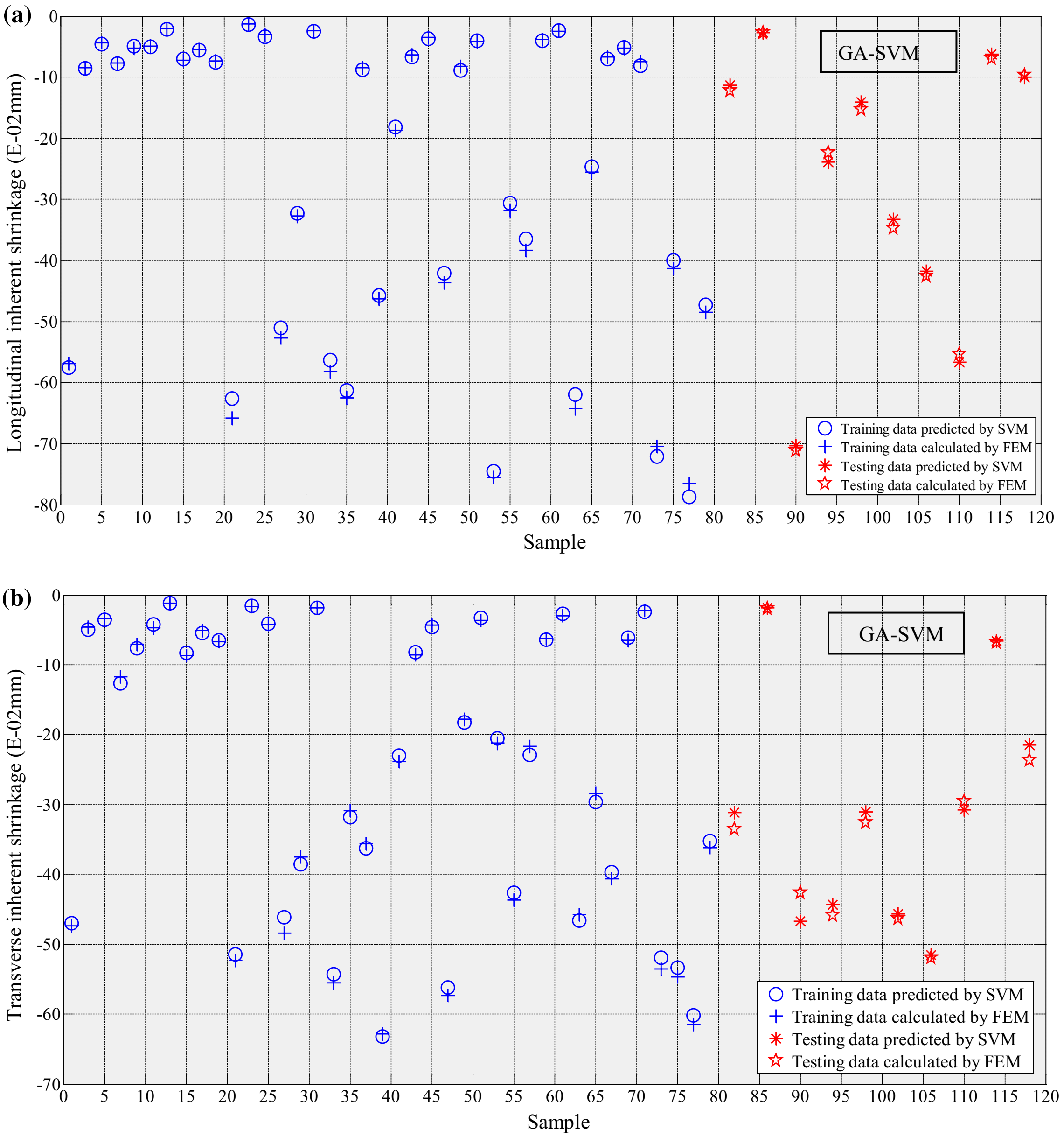

Fig. 17 Comparison between the predicted results by GA–SVM and calculated results by FEM: **a** longitudinal inherent deformation; **b** transverse inherent deformation

For the convenience of discussion, some professional sentences are simplified. There are two kinds of SVM models that are used for discussion and comparison, including the SVM model with optimal parameters obtained by the GA and the SVM model with the initial parameters of random selection. Then, the SVM model optimized by the GA is abbreviated as " GA–SVM ", the other SVM model, which is not optimized by the GA, refers to the common SVM model and is abbreviated as "CO–SVM". The SVM model for the inherent deformations was trained using the training samples obtained from the **TEP FE** simulation results, a number of data samples reserved as testing samples were used to verify the predicted accuracy of the SVM model. Therefore, some indexes need to be adopted to give a better illustration of the SVM model thus developed. In general, several standard statistical criteria have been employed to evaluate the prediction performance of the developed SVM model, such as mean absolute percentage error (MAPE), square correlation coefficient (SCC) and maximum percentage error (MPE). These statistical criteria are expressed as follows:

$$\mathrm{MAPE} = \frac{1}{N}\sum_{i=1}^{N}\left(\frac{|C_i - P_i|}{P_i}\right) \times 100\% \qquad (19)$$

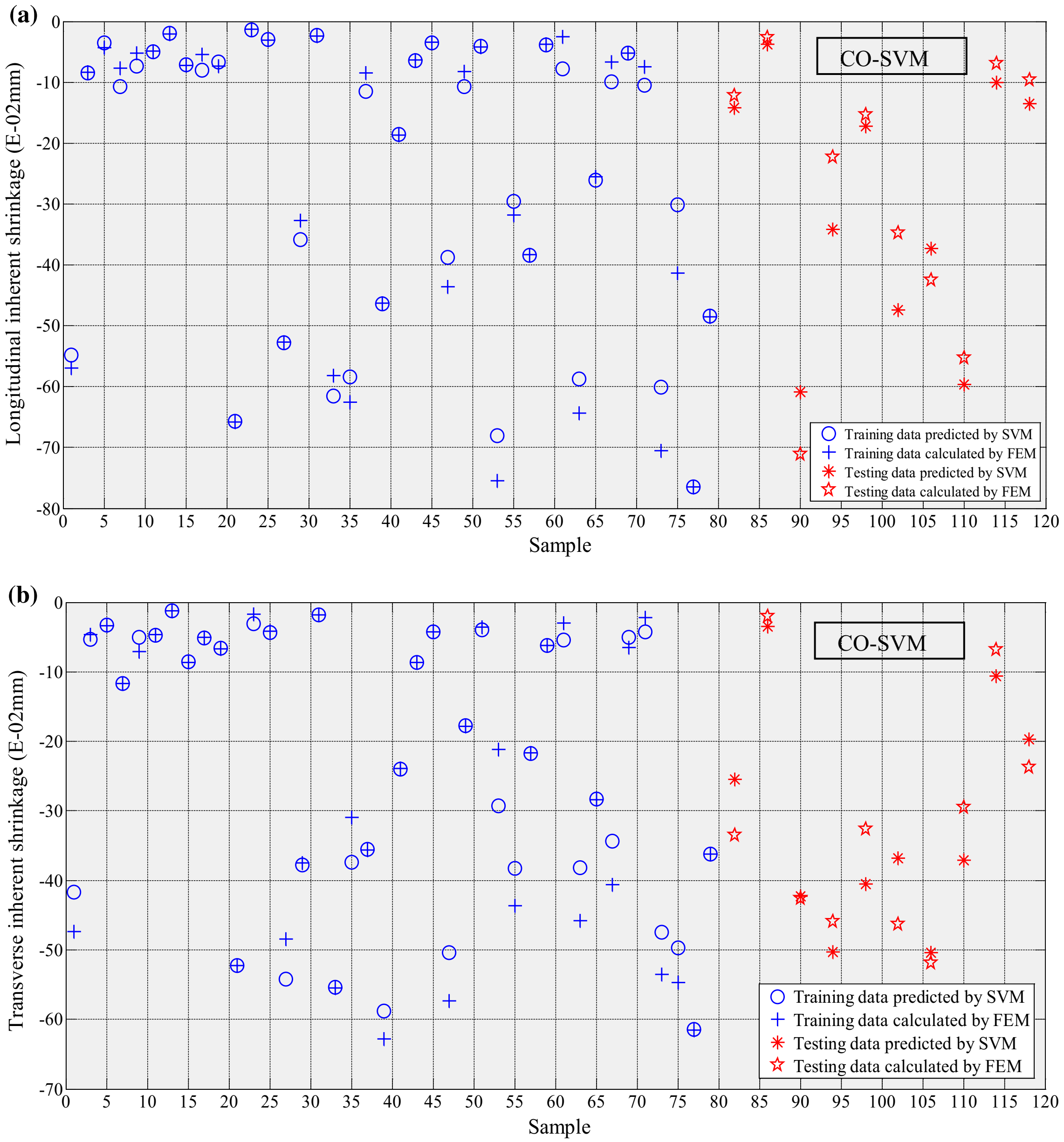

Fig. 18 Comparison between the predicted results by CO–SVM and calculated results by FEM: **a** longitudinal inherent deformation; **b** transverse inherent deformation

$$\mathrm{SCC}=\frac{\left(\sum_{i=1}^{N}\left(C_i-\bar{C}\right)\left(P_i-\bar{P}\right)\right)^2}{\sum_{i=1}^{N}\left(C_i-\bar{C}\right)^2\sum_{i=1}^{N}\left(P_i-\bar{P}\right)^2} \tag{20}$$

$$\mathrm{MPE}=\max_i\left[\left(\frac{C_i-P_i}{P_i}\right)\times 100\%\right] \tag{21}$$

where C and P are the calculated and predicted values of the inherent deformations, which are obtained by the finite element method and SVM model, respectively. $\bar{C}$ and $\bar{P}$ are the mean values of C and P, respectively. N represents the total number of training samples employed in the investigation.

It is necessary to point out that in these figures (Figs. 17, 18), the blue '○' represents the training sample data predicted by the SVM model, the blue '+' represents the training sample data calculated by **TEP FE** method, the red '*' represents the testing sample data predicted by the SVM model, the red '☆' represents the testing sample data calculated by the **TEP FE** method. A comparison plot between the predicted results by GA–SVM and the calculated results by FEM is shown in Fig. 17. It can be seen from Fig. 17 that when the GA–SVM model is used

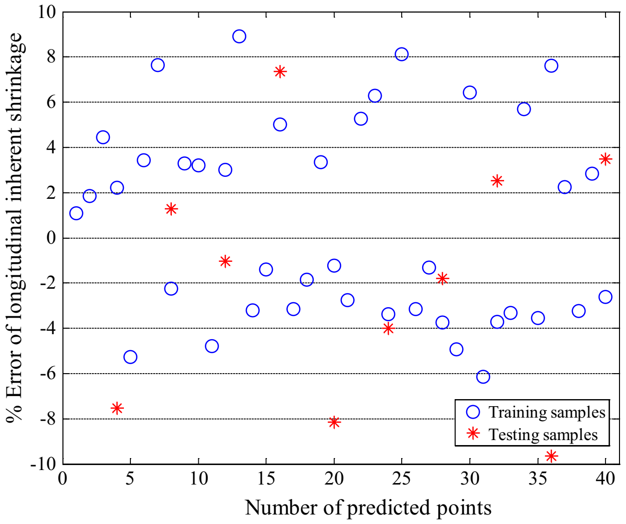

Fig. 19 Distribution of % error of predicted results using the GA–SVM model for longitudinal inherent deformation

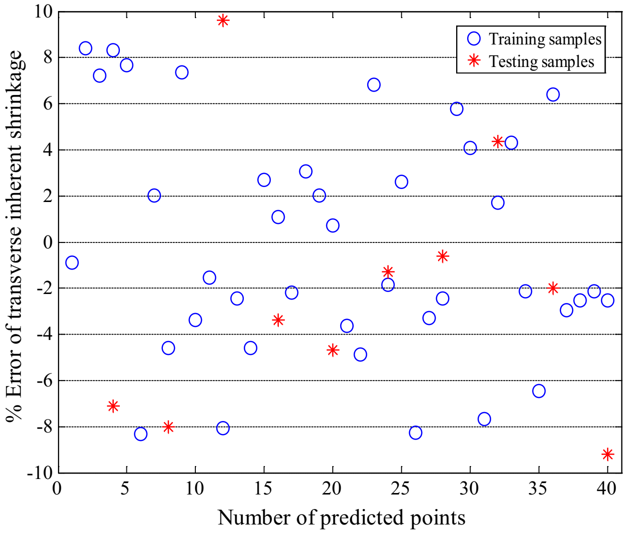

Fig. 20 Distribution of % error of predicted results using the GA–SVM model for transverse inherent deformation

to predict the inherent deformations, the predicted values by SVM are in good agreement with the simulation results by the **TEP FE** method for the majority of data points, whether it is for the longitudinal inherent deformation (as shown in Fig. 17a) or the transverse inherent deformation (as shown in Fig. 17b). As a comparison, Fig. 18 shows the data points distributions for the predicted values by CO–SVM model and calculated values by **TEP FE** method. It can be easily seen from Fig. 18 that the predicted values by CO–SVM are not well matched with the calculated values by the **TEP FE** method. Especially for the testing samples, the differences between the predicted and calculated values for the longitudinal and transverse inherent deformations are relatively larger. This indicates that the proposed SVM model with parameters optimized by the GA can significantly improve the prediction accuracy for both longitudinal and transverse inherent deformations.

The percentage difference is used to measure the spread of prediction error obtained by the GA–SVM model for all the samples in predicting the longitudinal and transverse inherent deformations. The percentage errors (%Error) are calculated by the following equation.

$$\%\text{Error} = \frac{\text{the input data} - \text{predicted results}}{\text{the input data}} \times 100 \tag{22}$$

Figures 19 and 20 show the percentage errors of the predicted results using the GA–SVM model for longitudinal and transverse inherent deformations, respectively. It is observed from the figures that the prediction error of the GA–SVM model to predict longitudinal and transverse inherent deformations for T-joint fillet welding is relatively uniform and well within an acceptable range. In general, the predicted values obtained from training samples are more accurate than those obtained by the testing samples due to the inherent characteristics of the supervised learning algorithm used in the SVM model. As can be seen from Fig. 19, the maximum error occurring when predicting the longitudinal inherent deformation is less than 8% for the most training samples, and the prediction errors of the testing samples are relatively larger, but also less than 10%. Similarly, the prediction errors of the transverse inherent deformation, most of which are less than 6% and 10% for training and testing samples, respectively, exhibit a distribution similar to that of longitudinal inherent deformation, just as shown in Fig. 20.

Table 7 Prediction performance evaluation of GA–SVM model for the inherent deformations

Training samples						Testing samples					
Transverse inherent deformation			Longitudinal inherent deformation			Transverse inherent deformation			Longitudinal inherent deformation		
MAPE	SCC	MPE	MAPE	SCC	MPE	MAPE	SCC	MPE	MAPE	SCC	MPE
4.226	0.998	8.414	3.923	0.998	8.924	5.026	0.995	9.618	4.681	0.996	9.639

MAPE (%) mean absolute percentage error, *SCC* square correlation coefficient, *MPE* (%) maximum percentage error

Table 7 gives the prediction performance evaluation of GA–SVM model for the inherent deformations based on the above mentioned statistical criteria. As shown in Table 7, for training samples, the maximum percentage errors of the longitudinal and transverse inherent deformations are 8.924% and 8.414%, respectively, while for the testing samples, the maximum percentage errors of the longitudinal and transverse inherent deformations are all about 9.6%, which are slightly larger than that of training samples. The correlation coefficient reflects the degree of correlation between predicted and simulation values. It can be observed that the SCC of 0.99 is obtained when predicting the longitudinal and transverse inherent deformations by the GA–SVM model, for both training and testing samples. The smaller differences of the MAPE between the training and testing samples demonstrate the GA–SVM model has a better generalization ability. As the SCC approaches 1 and the MAPE approaches 0, the model achieves better performance. This indicates that the GA–SVM model exhibits a considerably good prediction performance. Consequently, the proposed GA–SVM model can provide a reasonable estimation for the inherent deformations of T-joint fillet welding under appropriate welding input parameters.

Conclusion

This research paper explored the development of the **TEP FE** model and the GA-optimized SVM model for the prediction of inherent deformations in the T-joint fillet welding, and the following conclusions can be drawn on the basis of research results obtained:

- An uncoupled thermo-mechanical FE formulation was proposed to calculate the longitudinal and transverse inherent deformations in the T-joint fillet welding. The welding experiment was performed to verify the effectiveness of the **TEP FE** model developed. It can be found that the simulation values from the **TEP FE** model agree well with the measured values from the welding experiments. Thus the effective **TEP FE** model can be applied to the numerical experiments for obtaining the inherent deformations.
- The numerical experiments were planned and implemented based on the developed **TEP FE** model of T-joint. An SVM model optimized by the GA was trained well by using the informative data obtained from numerical experiments, which can give a better prediction for the longitudinal and transverse inherent deformations under a given range of welding input parameters. It can be concluded that the proposed GA–SVM model has a good generalization ability through the testing samples verification.
- It can be observed from the results that a correlation coefficient of about 0.99 was obtained between the predicted results from the GA–SVM model and the calculated results from the **TEP FE** model. Other statistical criteria also indicate that the GA–SVM model has a good prediction performance. In conclusion, the GA–SVM model developed in this study can serve as an effective predictor for the inherent deformations under a certain range of welding conditions.

The current researches were carried out for T-welded joint, and future research will focus on expanding to more types of welded joints and based on intelligent algorithms to establish a large-scale inherent deformation database, which can be applied to the rapid assessment of welding deformations of plate structures in shipbuilding and automotive industries.

Acknowledgements This research has been supported by the National Natural Science Foundation of China (NSFC) under Grant No. 51708346.

References

Ahmadzadeh, M., Fard, A. H., Saranjam, B., & Salimi, H. R. (2012). Prediction of residual stresses in gas arc welding by back propagation neural network. *NDT and E International, 52,* 136–143.

Ai, Y., Jiang, P., Shao, X., Wang, C., Li, P., Mi, G., et al. (2016). A defect-responsive optimization method for the fiber laser butt welding of dissimilar materials. *Materials and Design, 90,* 669–681.

Atabaki, M. M., Nikodinovski, M., Chenier, P., Ma, J., Liu, W., & Kovacevic, R. (2014). Experimental and numerical investigations of hybrid laser arc welding of aluminum alloys in the thick T-joint configuration. *Optics & Laser Technology, 59,* 68–92.

Ates, H. (2007). Prediction of gas metal arc welding parameters based on artificial neural networks. *Materials and Design, 28*(7), 2015–2023.

Baraka, A., Panoutsos, G., & Cater, S. (2015). A real-time quality monitoring framework for steel friction stir welding using computational intelligence. *Journal of Manufacturing Processes, 20,* 137–148.

Brickstad, B., & Josefson, B. L. (1998). A parametric study of residual stresses in multi-pass butt-welded stainless steel pipes. *International Journal of Pressure Vessels and Piping, 75*(1), 11–25.

Chaki, S., Shanmugarajan, B., Ghosal, S., & Padmanabham, G. (2015). Application of integrated soft computing techniques for optimisation of hybrid CO_2 laser-MIG welding process. *Applied Soft Computing, 30,* 365–374.

Chen, Z., Chen, Z., & Shenoi, R. A. (2015). Influence of welding sequence on welding deformation and residual stress of a stiffened plate structure. *Ocean Engineering, 106,* 271–280.

Chen, B. Q., & Soares, C. G. (2016). Effects of plate configurations on the weld induced deformations and strength of fillet-welded plates. *Marine Structures, 50,* 243–259.

Choobi, M. S., Haghpanahi, M., & Sedighi, M. (2012). Prediction of welding-induced angular distortions in thin butt-welded plates using artificial neural networks. *Computational Materials Science, 62,* 152–159.

Dabiri, M., Ghafouri, M., Raftar, H. R., & Björk, T. (2017). Neural network-based assessment of the stress concentration factor in a T-welded joint. *Journal of Constructional Steel Research, 128,* 567–578.

Das, B., Pal, S., & Bag, S. (2016). A combined wavelet packet and Hilbert-Huang transform for defect detection and modelling of weld strength in friction stir welding process. *Journal of Manufacturing Processes, 22,* 260–268.

Deng, D., Kiyoshima, S., Ogawa, K., Yanagida, N., & Saito, K. (2011). Predicting welding residual stresses in a dissimilar metal girth welded pipe using 3D finite element model with a simplified heat source. *Nuclear Engineering and Design, 241*(1), 46–54.

Deng, D., Liang, W., & Murakawa, H. (2007a). Determination of welding deformation in fillet-welded joint by means of numerical simulation and comparison with experimental measurements. *Journal of Materials Processing Technology, 183*(2–3), 219–225.

Deng, D., & Murakawa, H. (2008). Prediction of welding distortion and residual stress in a thin plate butt-welded joint. *Computational Materials Science, 43*(2), 353–365.

Deng, D., Murakawa, H., & Liang, W. (2007b). Numerical simulation of welding distortion in large structures. *Computer Methods in Applied Mechanics and Engineering, 196*(45–48), 4613–4627.

Deng, D., Murakawa, H., & Liang, W. (2008). Prediction of welding distortion in a curved plate structure by means of elastic finite element method. *Journal of Materials Processing Technology, 203*(1–3), 252–266.

Deng, D., Murakawa, H., & Shibahara, M. (2010). Investigations on welding distortion in an asymmetrical curved block by means of numerical simulation technology and experimental method. *Computational Materials Science, 48*(1), 187–194.

Deng, D., Sun, J., Dai, D., & Jiang, X. (2015). Influence of accelerated cooling condition on welding thermal cycle, residual stress, and deformation in SM490A steel ESW joint. *Journal of Materials Engineering and Performance, 24*(9), 3487–3501.

Dewan, M. W., Huggett, D. J., Liao, T. W., Wahab, M. A., & Okeil, A. M. (2016). Prediction of tensile strength of friction stir weld joints with adaptive neuro-fuzzy inference system (ANFIS) and neural network. *Materials and Design, 92,* 288–299.

Dey, V., Pratihar, D. K., Datta, G. L., Jha, M. N., Saha, T. K., & Bapat, A. V. (2009). Optimization of bead geometry in electron beam welding using a Genetic Algorithm. *Journal of Materials Processing Technology, 209*(3), 1151–1157.

Dhas, J. E. R., & Kumanan, S. (2016). Evolutionary fuzzy SVR modeling of weld residual stress. *Applied Soft Computing, 42,* 423–430.

Fu, G., Lourenço, M. I., Duan, M., & Estefen, S. F. (2016). Influence of the welding sequence on residual stress and distortion of fillet welded structures. *Marine Structures, 46,* 30–55.

Gao, Z., Shao, X., Jiang, P., Cao, L., Zhou, Q., Yue, C., et al. (2016). Parameters optimization of hybrid fiber laser-arc butt welding on 316L stainless steel using Kriging model and GA. *Optics & Laser Technology, 83,* 153–162.

Ghetiya, N. D., & Patel, K. M. (2014). Prediction of tensile strength in friction stir welded aluminium alloy using artificial neural network. *Procedia Technology, 14,* 274–281.

He, K., & Li, X. (2016). A quantitative estimation technique for welding quality using local mean decomposition and support vector machine. *Journal of Intelligent Manufacturing, 27*(3), 1–9.

Huang, W., & Kovacevic, R. (2011). A neural network and multiple regression method for the characterization of the depth of weld penetration in laser welding based on acoustic signatures. *Journal of Intelligent Manufacturing, 22*(2), 131–143.

Huang, Y., Wu, D., Zhang, Z., Chen, H., & Chen, S. (2017). EMD-based pulsed TIG welding process porosity defect detection and defect diagnosis using GA–SVM. *Journal of Materials Processing Technology, 239,* 92–102.

Islam, M., Buijk, A., Rais-Rohani, M., & Motoyama, K. (2015). Process parameter optimization of lap joint fillet weld based on FEM-RSM-GA integration technique. *Advanced Engineering Software, 79,* 127–136.

Jha, M. N., Pratihar, D. K., Bapat, A. V., Dey, V., Ali, M., & Bagchi, A. C. (2014). Knowledge-based systems using neural networks for electron beam welding process of reactive material (Zircaloy-4). *Journal of Intelligent Manufacturing, 25*(6), 1315–1333.

Jung, G. H., & Tsai, C. L. (2004). Fundamental studies on the effect of distortion control plans on angular distortion in fillet welded T-joints. *Welding Journal, 83*(7), 213–223.

Kang, K. W., Goo, B. C., Kim, J. H., Kim, D. K., & Kim, J. K. (2009). Experimental investigation on static and fatigue behavior of welded SM490A steel under low temperature. *International Journal of Steel Structures, 9*(1), 85–91.

Kanti, K. M., & Rao, P. S. (2008). Prediction of bead geometry in pulsed GMA welding using back propagation neural network. *Journal of Materials Processing Technology, 200*(1–3), 300–305.

Katherasan, D., Elias, J. V., Sathiya, P., & Haq, A. N. (2014). Simulation and parameter optimization of flux cored arc welding using artificial neural network and particle swarm optimization algorithm. *Journal of Intelligent Manufacturing, 25*(1), 67–76.

Kecman, V. (2001). *Learning and soft computing*. Cambridge, MA: MIT Press.

Koo, Y. D., Yoo, K. H., & Man, G. N. (2017). Estimation of residual stress in welding of dissimilar metals at nuclear power plants using cascaded support vector regression. *Nuclear Engineering and Technology, 49*(4), 817–824.

Liang, W., Murakawa, H., & Deng, D. (2016). Estimating inherent deformation in thin-plate Al-alloy joint by means of inverse analysis with the help of cutting technique. *Advanced Engineering Software, 99,* 89–99.

Lin, H. L. (2012). The use of the Taguchi method with grey relational analysis and a neural network to optimize a novel GMA welding process. *Journal of Intelligent Manufacturing, 23*(5), 1671–1680.

Ma, N., Huang, H., & Murakawa, H. (2015). Effect of jig constraint position and pitch on welding deformation. *Journal of Materials Processing Technology, 221,* 154–162.

Man, G. N., Jin, W. K., Dong, H. L., & Kang, Y. J. (2008). Residual stress prediction of dissimilar metals welding at NPPs using support vector regression. *Nuclear Engineering and Design, 238*(7), 1503–1510.

Mathew, J., Moat, R. J., Paddea, S., Fitzpatrick, M. E., & Bouchard, P. J. (2017). Prediction of residual stresses in girth welded pipes using an artificial neural network approach. *International Journal of Pressure Vessels and Piping, 150,* 89–95.

Mitchell, M. (1996). *An introduction to genetic algorithms*. Cambridge, MA: MIT Press.

Nagesh, D. S., & Datta, G. L. (2002). Prediction of weld bead geometry and penetration in shielded metal-arc welding using artificial neural networks. *Journal of Materials Processing Technology, 123*(2), 303–312.

Okuyucu, H., Kurt, A., & Arcaklioglu, E. (2007). Artificial neural network application to the friction stir welding of aluminum plates. *Materials and Design, 28*(1), 78–84.

Pal, S., Pal, S. K., & Samantaray, A. K. (2008). Artificial neural network modeling of weld joint strength prediction of a pulsed metal inert gas welding process using arc signals. *Journal of Materials Processing Technology, 202*(1–3), 464–474.

Pashazadeh, H., Gheisari, Y., & Hamedi, M. (2016). Statistical modeling and optimization of resistance spot welding process parameters using neural networks and multi-objective genetic algorithm. *Journal of Intelligent Manufacturing, 27*(3), 549–559.

Perić, M., Tonković, Z., Garašić, I., & Vuherer, T. (2016). An engineering approach for a T-joint fillet welding simulation using simplified material properties. *Ocean Engineering, 128,* 13–21.

Perić, M., Tonković, Z., Rodić, A., Surjak, M., Garašić, I., Boras, I., et al. (2014). Numerical analysis and experimental investigation of welding residual stresses and distortions in a T-joint fillet weld. *Materials and Design, 53,* 1052–1063.

Radaj, D. (1992). *Heat effects of welding: Temperature field, residual stress and distortion*. Berlin: Springer.

Sathiya, P., Panneerselvam, K., & Jaleel, M. Y. A. (2012). Optimization of laser welding process parameters for super austenitic stainless steel using artificial neural networks and genetic algorithm. *Materials and Design, 36,* 490–498.

Satpathy, M. P., Moharana, B. R., Dewangan, S., & Sahoo, S. K. (2015). Modeling and optimization of ultrasonic metal welding on dissimilar sheets using fuzzy based genetic algorithm approach. *Engineering Science and Technology, an International Journal, 18*(4), 634–647.

Shen, J., & Chen, Z. (2014). Welding simulation of fillet-welded joint using shell elements with section integration. *Journal of Materials Processing Technology, 214*(11), 2529–2536.

Sudhakaran, R., Murugan, V. V., & Sivasakthivel, P. S. (2012). Optimization of process parameters to minimize angular distortion in gas tungsten arc welded stainless steel 202 grade plates using particle swarm optimization. *Journal of Engineering Science and Technology, 7*(2), 195–208.

Tarng, Y. S., Wu, J. L., Yeh, S. S., & Juang, S. C. (1999). Intelligent modelling and optimization of the gas tungsten arc welding process. *Journal of Intelligent Manufacturing, 10*(1), 73–79.

Teimouri, R., & Baseri, H. (2015). Forward and backward predictions of the friction stir welding parameters using fuzzy-artificial bee colony-imperialist competitive algorithm systems. *Journal of Intelligent Manufacturing, 26*(2), 1–13.

Tian, L., Luo, Y., Wang, Y., & Wu, X. (2014). Prediction of transverse and angular distortions of gas tungsten arc bead-on-plate welding using artificial neural network. *Materials and Design, 54,* 458–472.

Ueda, Y., & Ma, N. X. (1994). Measuring method of three dimensional residual stress with aid of distribution function of inherent strain. *Transactions of JWRI, 23*(1), 123–130.

Ueda, Y., Murakawa, H., & Ma, N. (2012). *Welding deformation and residual stress prevention*. Butterworth Heinemann: Elsevier Publishing.

Ueda, Y., Murakawa, H., Nakacho, K., & Ma, N. X. (1995). Establishment of computational welding mechanics. *Transactions of JWRI, 24*(2), 73–86.

Ueda, Y., & Yuan, M. G. (1993). Prediction of residual stresses in butt welded plates using inherent strains. *Journal of Engineering Materials and Technology, 115*(4), 417–423.

Vakili-Tahami, F., & Ziaei-Asl, A. (2013). Numerical and experimental investigation of T-shape fillet welding of AISI 304 stainless steel plates. *Materials and Design, 47*(9), 615–623.

Vapnik, V. (1995). *The nature of statistical learning theory*. New York: Springer.

Vetriselvan, R., Devakumaran, K., Sathiya, P., & Ravichandran, G. (2017). Transient out-of-plane distortion of multi-pass fillet welded tube to pipe T-joints. *Defence Technology, 13*(2), 77–85.

Wang, J. (2012). *Investigation of buckling distortion of ship structure due to welding assembly using inherent deformation theory*. Doctoral thesis, Osaka University.

Wang, J., Rashed, S., & Murakawa, H. (2014). Mechanism investigation of welding induced buckling using inherent deformation method. *Thin-Walled Structures, 80,* 103–119.

Wang, J., Rashed, S., Murakawa, H., & Luo, Y. (2013a). Numerical prediction and mitigation of out-of-plane welding distortion in ship panel structure by elastic FE analysis. *Marine Structures, 34,* 135–155.

Wang, J., Yin, X., & Murakawa, H. (2013b). Experimental and computational analysis of residual buckling distortion of bead-on-plate welded joint. *Journal of Materials Processing Technology, 213*(8), 1447–1458.

Wang, J., Yuan, H., Ma, N., & Murakawa, H. (2016). Recent research on welding distortion prediction in thin plate fabrication by means of elastic FE computation. *Marine Structures, 47,* 42–59.

Wang, R., Zhang, J., Serizawa, H., & Murakawa, H. (2009). Study of welding inherent deformations in thin plates based on finite element analysis using interactive substructure method. *Materials and Design, 30*(9), 3474–3481.

Wang, J., Zhao, H., Zou, J., Zhou, H., Wu, Z., & Du, S. (2017). Welding distortion prediction with elastic FE analysis and mitigation practice in fabrication of cantilever beam component of jack-up drilling rig. *Ocean Engineering, 130,* 25–39.

Wu, D., Chen, H., Huang, Y., He, Y., Hu, M., & Chen, S. (2017). Monitoring of weld joint penetration during variable polarity plasma arc welding based on the keyhole characteristics and PSO-ANFIS. *Journal of Materials Processing Technology, 239,* 113–124.

Zhang, Y., Gao, X., & Katayama, S. (2015). Weld appearance prediction with BP neural network improved by genetic algorithm during disk laser welding. *Journal of Manufacturing Systems, 34,* 53–59.